




A Passive, Fully Staring THz Video Camera Based on Kinetic Inductance Bolometer Arrays

Juho Luomahaara , Hannu Sipola, Leif Grönberg , *Life Member, IEEE*, Aki Mäyrä, Mika Aikio, Andrey Timofeev , Kirsi Tappura , Anssi Rautiainen, Alekski Tamminen , Visa Vesterinen , Mikko Leivo, Feng Gao , Hannu Vasama, Arttu Luukanen , and Juha Hassel

Abstract—Current state-of-the-art security video cameras operating in the THz regime employ up to a few hundred detectors together with optomechanical scanning to cover an adequate field-of-view for practical concealed object detection. As a downside, the scanning reduces the integration time per pixel compromising sensitivity, increases the complexity, and reduces the reliability of the system. In contrast to this, we demonstrate a video camera, for the first time, basing its operation on the concept of a fully staring 2-D detector array with a single detector element responsible for a single imaged pixel. The imaging system is built around the detector technology of kinetic inductance bolometers, allowing the operation in the intermediate temperature range >5 K and the scale-up of the detector count into multikilo-pixel arrays and beyond. The system is designed for a field-of-view of 2×1 m² and an imaging distance of 2.5 m. We describe the main components of the system and

show images from concealed object experiments performed at a near-video rate of 9 Hz.

Index Terms—Bolometer, focal plane array (FPA), kinetic inductance, radiometry, security screening, THz imaging, THz video camera.

I. INTRODUCTION

ALTHOUGH the idea of using subterahertz radiation for concealed object detection is not a new one [1], the lack of available instrumentation in this frequency range for long delayed the development of applicable imaging systems. The transmission through dielectric materials, including the most common clothing, deteriorates with increasing frequency and is very small already at 1 THz [2], defining the upper limit of the frequency band of interest. On the other hand, the achievable spatial resolution fundamentally scales with the wavelength, making standoff detection unattractive below a few hundred gigahertz. The active video cameras operating in the optimal regime illuminate targets with high-power sources, making the detection with room-temperature detectors adequate [3]. In passive imaging, the magnitude of the signal is limited by the scene and requirements for detector sensitivity are more pronounced. The power of radiation emitted by room-temperature objects is 4–5 orders of magnitude smaller in the 0.2–1 THz band than at 20 THz where the spectrum of Planck’s blackbody spectral radiance peaks. To achieve the required sensitivity, the conventional passive imagers are based on cooled bolometers although competing detectors operating at room temperature are also being developed [4].

Due to their similar nature of operation, the advances made in space instrumentation have supported also the development of passive imaging systems for terrestrial applications. Passive video cameras based on both transition edge sensors [5] and kinetic inductance detectors (KIDs) [6] have been reported. The common denominator for these systems is that they are operated below 0.5 K. However, for commercial applications, it becomes increasingly important to find technological solutions that are cost-efficient and robust. The prior work at VTT has concentrated on developing passive imaging technology with affordable cryogenics operating in the temperature range of 5–10 K [7]. The imager utilizes the so-called hot-spot bolometers [8], based on the resistive transition [9] in a voltage-biased superconducting air bridge, combined with room-temperature readout electronics. These imaging systems are today commercially available

Manuscript received June 30, 2020; revised September 8, 2020; accepted September 25, 2020. Date of publication October 19, 2020; date of current version January 5, 2021. This work was supported in part by the European Space Agency (ESA) under Contract GSTP 4000115091/15/NL/AF “Large-area staring kinetic inductance focal plane array operating at elevated temperature” and in part by the Academy of Finland under Grant 314447 and Grant 317844. (Corresponding author: Juho Luomahaara.)

Juho Luomahaara, Hannu Sipola, Leif Grönberg, Kirsi Tappura, and Visa Vesterinen are with Quantum Systems, VTT Technical Research Centre of Finland Ltd., QTF Centre of Excellence, VTT FI-02044, Finland (e-mail: Juho.Luomahaara@vtt.fi; Hannu.Sipola@vtt.fi; Leif.Gronberg@vtt.fi; Kirsi.Tappura@vtt.fi; Visa.Vesterinen@vtt.fi).

Aki Mäyrä and Hannu Vasama are with Optical Measurements, VTT Technical Research Centre of Finland Ltd., VTT FI-02044, Finland (e-mail: Aki.Mayra@vtt.fi; hannu.vasama@vtt.fi).

Feng Gao is with MEMS, VTT Technical Research Centre of Finland Ltd., FI-02044 VTT, Finland (e-mail: feng.gao@vtt.fi).

Mika Aikio was with the VTT Technical Research Centre of Finland Ltd., VTT FI-02044, Finland. He is now with Displex Oy, FI-02130 Espoo, Finland (e-mail: Mika.Aikio@displex.com).

Andrey Timofeev was with the VTT Technical Research Centre of Finland Ltd., VTT FI-02044, Finland. He is now with Australian Research Council Centre of Excellence for Quantum Computation and Communication Technology, School of Physics, University of New South Wales, Sydney NSW 2052, Australia (e-mail: Andrey.Timofeev@unsw.edu.au).

Anssi Rautiainen and Arttu Luukanen are with Asqella Oy, FI-00380 Helsinki, Finland (e-mail: Anssi.Rautiainen@asqella.com; arttu.luukanen@asqella.com).

Alekski Tamminen was with the Asqella Oy, FI-00380 Helsinki, Finland. He is now with Department of Electronics and Nanoengineering, Aalto University, FI-02150 Espoo, Finland (e-mail: Alekski.Tamminen@aalto.fi).

Mikko Leivo was with the Asqella Oy, FI-00380 Helsinki, Finland. He is now with Mectalent Oy, FI-90620 Oulu, Finland (e-mail: Mikko.Leivo@mectalent.fi).

Juha Hassel was with the VTT Technical Research Centre of Finland Ltd., VTT FI-02044, Finland. He is now with IQM Quantum Computers, FI-02150 Espoo, Finland (e-mail: Juha.Hassel@meetiqm.com).

Color versions of one or more of the figures in this article are available online at <https://ieeexplore.ieee.org>.

Digital Object Identifier 10.1109/TTHZ.2020.3029949

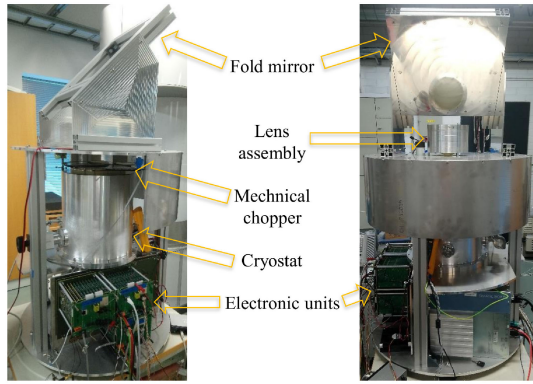


Fig. 1. LASTKID imaging system shown from the side (left panel) and from the imaging direction (right panel) with some of its subsystems indicated.

[10]. All the above-mentioned video cameras contain up to a few hundred detectors and employ optomechanical scanning to cover an adequate field-of-view (FOV) for security screening. As a downside, the system sensitivity is degraded roughly with a factor of $N_{\text{eff}}^{1/2}$, where N_{eff} is the number of pixels acquired with a single detector.

In this article, we present a fully staring passive THz imaging system, i.e., a video camera without scanning mechanics where each detector produces a single pixel in the image. The cornerstone of the “LASTKID” imager is the detector technology based on the so-called kinetic inductance bolometers (KIBs) developed at VTT [11] that allow the fabrication and readout of high-pixel-count focal plane arrays (FPAs) and operation in the intermediate temperature range above 5 K. In contrast to their millikelvin counterparts, i.e., KIDs [12] relying on nonequilibrium excitation of quasiparticles, KIBs exploit the temperature dependence of kinetic inductance in thermal equilibrium with the design resembling those presented in [13] and [14]. We have previously demonstrated the operation of single KIBs [11] and large detector arrays [15] as well as their readout [16] in the sensitivity level needed for radiometric imaging for terrestrial applications. Here, a full imaging system is described. After presenting the main design guidelines and characteristics of the imaging system, the imaging performance is measured in terms of optical resolution and radiometric contrast. Furthermore, we show video imagery from practical concealed object detection experiments performed with a frame rate of 9 Hz and FOV of $0.66 \times 0.86 \text{ m}^2$. We conclude by discussing the future prospects of the presented technology.

II. IMAGING SYSTEM

The LASTKID imaging system is shown in Fig. 1. The imager operates at $T = 5.8 \text{ K}$ using a closed-cycle Gifford–McMahon cryocooler, enclosing the FPA inside. THz radiation is able to access the cryostat through a rather large optical window with the approximate dimensions of the focal plane $100 \text{ mm} \times 200 \text{ mm}$. The sufficient infrared (IR) rejection is achieved by combining thermal filters, such as those described in [17], and Zitex polymer filters [18], defining the instrument bandwidth to 1 THz. The main components of the system are the detector array, readout electronics, and optics which will be described in the sections

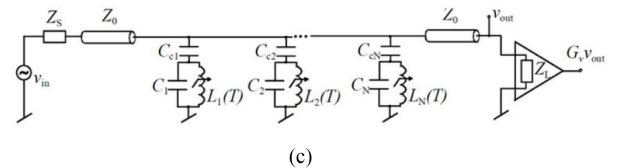
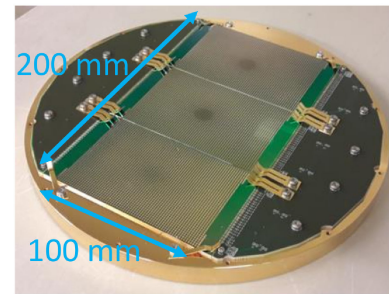
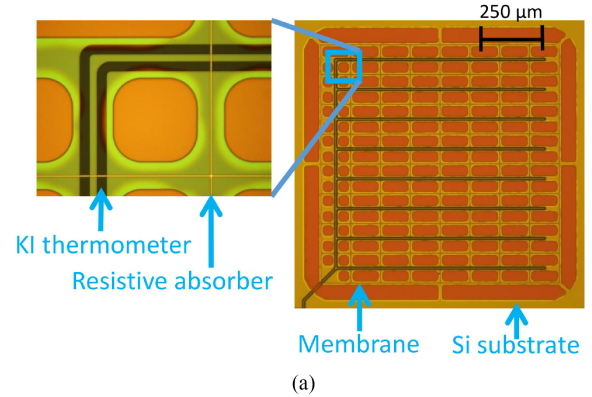


Fig. 2. (a) Optical photograph of the kinetic inductance bolometer. The main components of the bolometer, resistive absorber, and kinetic inductance thermometer are patterned on a 300-nm-thick SiN membrane which has been released from the back side with through-wafer etching process on areas shown with orange color. As a result, the membrane has low heat capacitance c and is thermally isolated from the Si substrate with eight narrow legs determining thermal conductance G . The TiW absorber has the shape of a square grid while the thermometer fabricated from NbN meanders along the membrane. The size of the membrane $W = 1 \text{ mm}$ and detectors are fabricated with a pitch $p = 1.5 \text{ mm}$. (b) Focal plane array with dimensions $A_{\text{FPA}} = 100 \times 200 \text{ mm}^2$. (c) Readout circuit for an array of kinetic inductance bolometers with temperature-dependent inductances serving as detector elements.

below. The total height of the instrument is about 130 cm with a footprint diameter of 65 cm. The system weight is 80 kg.

A. Detector Array

The main features of the KIB technology have been reported before [11], [15], [19]. The detector array for the LASTKID imaging system follows these design principles. The structure of the KIB is shown in Fig. 2(a). A resistive absorber converts the power of THz radiation into heat on a membrane. Optimal radiation coupling is achieved by matching the sheet resistance of the absorbing material to the vacuum impedance of 377Ω . The coupling can be enhanced further with a reflective element located at a distance $h_{\text{bs}} = n\lambda/4$ behind the detector, where n is an odd integer and λ the wavelength of the radiation in the medium. We used a metallic cold finger as the backshort with $h_{\text{bs}} = 450 \mu\text{m}$ as defined by the thickness of the Si wafer. The heat-induced change of temperature is then detected utilizing the temperature dependence of the kinetic inductance of the

a superconducting NbN meander. Here it is assumed that the membrane itself together with the absorber and the thermometer are in thermal equilibrium.

The focal plane of the LASTKID is shown in Fig. 2(b). It contains three tiles, each fabricated on a single 150 mm Si wafer. The total detector count $N_{\text{tot}} = 8712$ that have been divided into 66 channels. The electrical scheme of one such channel is shown in Fig. 2(c). Inductor L_i with $i = 1, \dots, 132$, containing contributions from geometric and kinetic inductances, is placed in parallel with an off-membrane capacitor C_i . The formed electrical resonator is further coupled to a transmission line with coupling capacitor C_{ci} , leading to a characteristic resonance frequency $f_i = 1/(2\pi\sqrt{L_i(C_i + C_{ci})})$ for each detector in the channel. To increase the packing density of the capacitors, we used atomic layer deposited aluminum oxide as the dielectric material with the relative permittivity of 8.5. It is to be noted that the measurements in this article were performed with $N = 114$ detectors per channel.

B. Readout

A detailed description of the serial addressed frequency excitation (SAFE) readout for the LASTKID is given in [16]. For completeness, a brief summary on the basic readout principles is given here. During a frame time τ_F , each detector in a channel is addressed sequentially in a time slot of $\tau_s = \tau_F/N$ with a corresponding resonance frequency f_i . As driven through the KIB array, the carrier signal gets modulated by the detector signals. The modulated signal is amplified at room temperature (noise temperature $T_N = 35$ K) and demodulated to the baseband, yielding the time-multiplexed detector signals for post-processing. The chosen readout band $f_{\text{BW}} = 20\text{--}300$ MHz is a compromise of two factors. The resonator quality factor decreases as a function of frequency [15], being small at the high frequency bound while the electrical response time of the resonator becomes too slow for multiplexing at low frequencies [16].

The benefit of SAFE is that high-speed digital electronics is only needed to generate the sinusoidal excitation tones as compared to the full frequency division multiplexing case [20], making the readout system drastically less expensive. It was also shown in [16] that in the ideal case of the phonon noise [21] being the dominant noise mechanism, SAFE does not degrade the multiplexed signal-to-noise ratio (SNR) as compared to the continuous readout of a single detector.

C. Optics

In many typical imaging applications, the available space is a limiting factor. Furthermore, wide FOV is preferred which sets specific requirements for the optics. This aspect has been previously addressed by a dual polymer lens structure in [22]. In the LASTKID system, we apply a slightly different concept based on a double-Gauss type lens assembly [23] with the FOV of 2 m diameter as limited by the optics. The imaging distance of the system is 2.55 m as measured from the imaging system center, including also the effect of the planar mirror bending the optical path by 90° . This allows easy flow of people while the system does not occupy too much footprint. A ray tracing simulation is illustrated in Fig. 3(a), along with a photograph of

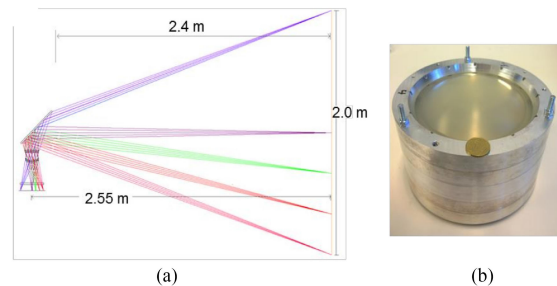


Fig. 3. (a) Ray tracing image of the optics showing the object plane on the right. The image is formed on the FPA under the lens system, whose physical realization is illustrated in (b).

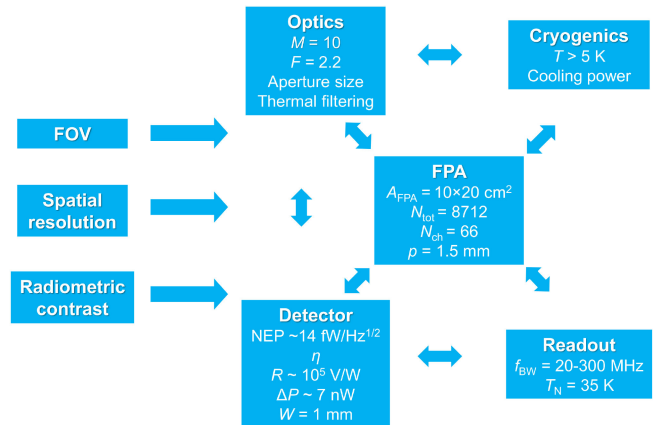


Fig. 4. Generic block diagram describing the optimization of the imaging system. Also the main specifications of the LASTKID imaging system are summarized.

the realized lens assembly in Fig. 3(b). Here TPX plastics was used as lens material. The optics has a magnification $M = 10$ from the focal plane to the object plane, and an f -number $F = 2.2$. Thus, the size of the focal plane 200 mm \times 100 mm limits here the final imaging area to 2 m \times 1 m. A mechanical chopper shown in Fig. 1 is placed between the cryostat window and the lens assembly, converting the base-band video signal to around the chopping frequency. Roughly speaking, this means that the signal is transformed to a root mean square value of a sinusoid having a peak-to-peak amplitude equivalent to the original dc signal level, leading to the loss of signal with a factor of $2\sqrt{2}$. The benefit is that the influence of low-frequency noise and thermal drifts in the cryostat are effectively eliminated, improving the total SNR of the measurement.

III. INSTRUMENT DESIGN OPTIMIZATION

The most important parameters specifying the imager performance are FOV, spatial resolution, and radiometric contrast which give rise to the tradeoffs between different subsystems of the instrument. The aim here is to present a simplified analysis, yielding basic design principles for the whole imaging system. Fig. 4 summarizes the basic figure of merits of the subsystems and their relationships.

Diffraction-limited spatial resolution Δx as defined by the full width at half maximum (FWHM) of an Airy disk and referred to the object plane is

$$\Delta x = 1.028M\lambda F. \quad (1)$$

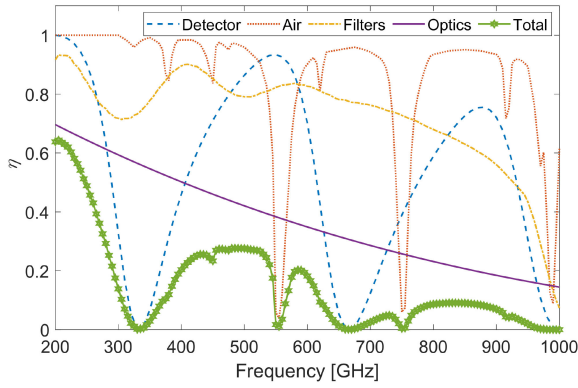


Fig. 5. Efficiencies from transmission and reflection losses due to IR filters and optical components together with atmospheric attenuation and optical coupling of the detector. These were estimated following the methodology presented in [15], supported by the transmission measurements performed for optical components in the THz regime. The detector efficiency was computed as the ratio of the absorbed power P_{abs} with respect to the area integral of the power density over the membrane. The total efficiency η is the product of other efficiency components.

For a spatially fully sampled system, the criterion for detector spacing is $p \leq 0.5\lambda F$ [24] and the requirements for the total detector count $N_{\text{tot}} = 4 \times \text{FOV}/(M\lambda F)^2$ and FPA area $A_{\text{FPA}} = \text{FOV}/M^2$. Clearly, low magnification and f -number promote high spatial resolution. Yet, this comes with the cost of a larger A_{FPA} and N_{tot} , increasing the cryogenic exposure to ambient IR load, silicon area in detector production, and complexity of the readout system. Very low f -numbers also challenge the optics design in maintaining the diffraction-limited resolution across the focal plane [22].

The radiometric contrast is quantified with the noise equivalent temperature difference (NETD) given by

$$\text{NETD} = \frac{\text{NEP}}{\partial P_{\text{abs}}/\partial T_s \sqrt{\tau}} = \frac{\text{NEP}}{2k_{\text{B}} \int_{f_1}^{f_2} \eta(f) \frac{A_{\text{det}} \Omega}{\lambda(f)^2} df \sqrt{\tau}} \quad (2)$$

where Rayleigh–Jeans approximation has been used in the last stage. Here, P_{abs} is the power received from a thermal source at temperature T_s , τ is the integration time of the measurement and NEP stands for noise equivalent power. The total efficiency η takes into account the different loss mechanisms present in the optical path as estimated in Fig. 5, with major losses stemming from the thermal filtering and optical components. A valid approximation for the normalized optical throughput is $A_{\text{det}} \Omega/\lambda^2 = \pi A_{\text{det}}/(4F^2 \lambda^2)$ [24], where Ω is the angle looking into the optics. With (2), we note that a low f -number also promotes better radiometric contrast. Furthermore, it appears favorable to increase the bandwidth toward the high-frequency end as the factor A_{det}/λ^2 increases quadratically with frequency, following from the frequency dependence of the blackbody irradiance [15]. However, the benefit of expanding the bandwidth is counteracted by the increase of dielectric losses in the optics and filters as apparent from the data of Fig. 5. Here we have assumed that the detector effective area $A_{\text{det}} \simeq W^2$ with W the absorber width. Although strictly valid only in the geometric limit $W/\lambda \gg 1$ [25], this is a good approximation with minor deviations at the low-frequency end of the spectrum [26].

The phonon noise across thermal link G dominates the detector noise, i.e., noise equivalent power $\text{NEP} = \sqrt{4k_{\text{B}} T^2 G}$, where k_{B} is the Boltzmann constant and T is the temperature. This noise is band limited with a cutoff frequency $f_c = G/(2\pi c)$. Thus, thermal conductance G and heat capacitance c determine the tradeoff between the detector speed and sensitivity. A rough optimization process, assuming c is determined by A_{det} and G is engineered to achieve sufficiently fast response time [19], yields $\text{NEP} \propto \sqrt{A_{\text{det}}}$. From this and (2), we further obtain $\text{NETD} \propto 1/\sqrt{A_{\text{det}}}$. Ideally, the maximum detector dimension $\sqrt{A_{\text{det}}} = p$, where detector pitch p is determined by the spatial sampling. Due to the fabrication tolerances, the detector pitch $p > W$ in practice.

For the detector readout, an important parameter is the power-to-voltage responsivity $R = \partial v_{\text{out}}/\partial P_{\text{abs}}$, which gives the noise power spectral density at the input of the preamplifier $S_{v,\text{out}} = (R \times \text{NEP})^2$. This can be converted into equivalent noise temperature $T_e = S_{v,\text{out}}/(k_{\text{B}} Z_{\text{L}})$, where Z_{L} is the preamplifier input impedance. The detector noise preferably dominates over amplifier noise. For the SAFE multiplexing scheme, this leads to a limiting condition for the detector count N in a channel given by $(R \times \text{NEP})^2/(k_{\text{B}} Z_{\text{L}} N) > T_{\text{N}}$, where T_{N} is the noise temperature of the preamplifier [16]. Detector count N is also affected by the dynamic range ΔP of the detectors [16]. By requiring that the change of the resonance frequency stays below the linewidth of the resonator and adjacent resonant frequencies are separated by several linewidths, it is straightforward to determine the maximum number of N for a given readout band f_{BW} . This also gives a preferred value for the number of channels as $N_{\text{ch}} = N_{\text{tot}}/N$, which, in turn, determines the heat loss due to wiring.

Based on these principles, the justification for the parameter choices is roughly as follows: The focal plane (or optical aperture) area was maximized based on the realizable thermal IR filtering and detector array. The IR load scale is set by the ambient blackbody radiation level estimated from the Stefan–Boltzmann law $P_{\text{rad}} = A_{\text{win}} \sigma T^4$, where $\sigma = 5.7 \times 10^{-8} \text{ W m}^{-2} \text{ K}^{-4}$. While the load can be, to an extent, reduced by reflective filters, the first cooling stage of the cryostat absorbs a large fraction of the radiation in practice. The particular aperture size A_{win} was chosen based on the comparison of the estimated ambient IR load $P_{\text{rad}} = 8 \text{ W}$ and the cooling power of the cryostat. The resulting FPA area $A_{\text{FPA}} = A_{\text{win}}$ was also compatible with the manufacturing criteria, enabling FPA production on three 150 mm silicon wafers. Furthermore, it was found that the double-Gaussian lens assembly with $F = 2.2$ and $M = 10$ can provide a near-diffraction limited spot size at the wavelength of $600 \mu\text{m}$ over the FOV of $2 \times 1 \text{ m}^2$. Finally, we note that with reference to the frequency band of interest, the chosen detector pitch $p = 1.5 \text{ mm}$ is a factor of 1–4.5 more sparse than the full sampling criterion, as a consequence of the detector and readout realizability. The ratio of the total optically active area with respect to the total FPA area is $A_{\text{det}}/p^2 = 0.44$. According to the above discussion, this approximately degrades the NETD by a factor $p/W = 1.5$ as compared to the case of an equal pitch and ideal filling $p = W$.

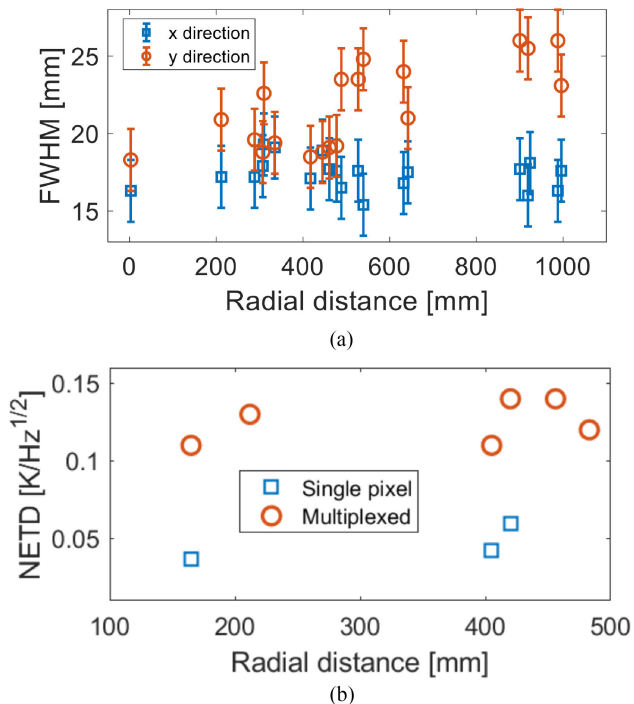


Fig. 6. (a) Full width at half maximum values measured as a function of the radial distance from the center of the object plane for x - and y -directions. (b) NETD values were determined for single pixels with full integration time $\tau_s = \tau_F$ and multiplexed case with $\tau_s = \tau_F/N$ over $N = 114$ detectors. As a result of multiplexing, the noise level increases from 0.04–0.06 to 0.11–0.14 K/Hz^{1/2}.

IV. MEASUREMENTS

A. System Characterization

The optical performance of the imaging system was characterized in terms of spatial resolution and radiometric contrast. The measurements followed the methodology presented in [15]. Unlike in imaging experiments, the optical chopper was placed in front of thermal sources, and not below the lens system shown in Fig. 1. The chopper was operated between 30 and 45 Hz. The recorded data was Fourier transformed, yielding the signal at chopping frequency.

The spatial resolution was measured by moving a hot-spot source along the object plane with an xy -manipulator. To quantify the optical resolution, the FWHM value of the point spread function is shown in Fig. 6(a). In the middle of the FPA, the spot size is around 16–18 mm. This can be compared to (1), which gives a correspondence to diffraction-limited performance with a point frequency of 400 GHz while the comparison to truly wide-band detection is more involved [27]. However, the spots become asymmetrical toward the FPA edge which can be seen as an increase of the FWHM value in y -direction, yet being well below 30 mm for the whole FOV.

The radiometric contrast was determined using an aqueous blackbody calibrator (ABC) [28] as a thermal source. The results are summarized in Fig. 6(b). Here, the NETD was measured only for radial distances below 500 mm as the blackbody emission from ABC is too narrow to cover the entire FOV of the imaging system. We estimate detector NEP of 14 fW/Hz^{1/2} based on the comparison of current and old detector designs and scaling from

the measurement data of the latter [11]. With this and efficiencies shown in Fig. 5, the computation of (2) yields theoretical NETD = 10 mK/Hz^{1/2}. Taking into account the loss of the signal due to chopping, NETD value of 28 mK/Hz^{1/2} is obtained which is in a reasonable agreement with the lowest measured value.

It is seen that noise increases with a factor of 2–3 upon multiplexing over $N = 114$ detectors. The origin of this multiplexing penalty stems from two factors [16]. First, the band-limited detector noise does not fully dominate over other wide-band noise sources such as those stemming from the excitation and readout electronics. Also, the Nyquist sampling criterion $f_F = 1/\tau_F > 2f_c$ is not met with the current design values of $f_c = 120$ Hz and $f_F = 146$ Hz. Still, the multiplexing is clearly beneficial as compared to the case of mechanical scanning suffering from the worst-case noise penalty $\sqrt{N} \sim 11$.

B. Imaging Experiments

The imaging capability of the LASTKID system was verified in concealed object detection experiments. Fig. 7(a)–(d) shows snapshots of video imagery taken from different imaging scenarios. Plastic rods made of polyoxymethylene (POM) were hidden against the test person’s back under a hooded shirt. Optical signal was chopped at 37 Hz while the data was recorded simultaneously from 20 channels corresponding to a detector count of 2280 and imaging area of 86×66 cm². Slot time τ_s was adjusted to 60 μ s leading to a frame time $\tau_F = 6.8$ ms for $N = 114$ detectors.

Except for the two missing channels indicated with green arrows in Fig. 7(a)–(d), the detector yield was generally found to be better than 97% in channels over the whole imaging area. The detector readout was tuned with the methodology described in [16], providing the excitation parameters and the encoding of the detector readout frequencies into the corresponding spatial coordinates. The nonidealities in the calibration process lead to discrete errors in the x -coordinate that is defined by the detector index within the channel. To fix these, we used a plastic pipe filled with hot water as a calibrator. The vertically aligned pipe was slowly moved horizontally with the xy -manipulator, providing a reference signal for spatial calibration of the detectors. Furthermore, as another calibration step, a copper plate was placed on top of the lens system [Fig. 3(b)] to provide a rough calibration method for varying detector responsivities.

To produce the image quality shown in Fig. 7, the procedure for data processing was the following. First, the data was demultiplexed and demodulated to the baseband using the chopping frequency as a local oscillator. The data was then averaged to the final video frame rate of 9 Hz after which the offset of the signal was subtracted. A compressor recycles He gas in cycles of 1 Hz to the cold stage of the cryocooler, creating thermal interference to the signal at this frequency and its multiples. The effect of this interference was removed as a next step. With the aid of acquired calibration data, the pixels were spatially reorganized and corresponding detector signals normalized. Finally, videos were produced using gamma correction with an exponent of 2.32 for color scale.

The 30-mm-wide rod is clearly visible in the imagery and even the 16-mm-wide rod hidden under the shirt is recognizable. Also

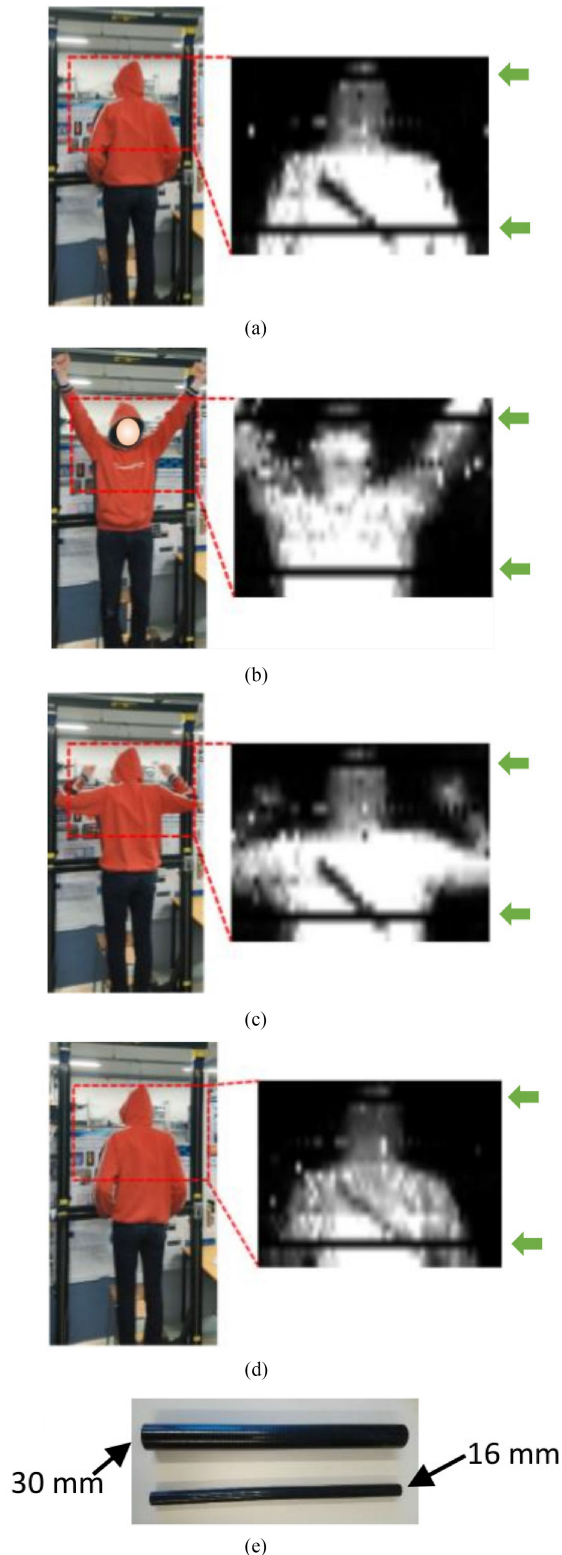


Fig. 7. (a)–(d) Snapshots from THz video imagery taken with the LASTKID imaging system and compared against optical imagery acquired with a mobile phone camera in different imaging positions. Rod-shaped items are concealed under the clothing of the test person’s back while there are no objects hidden on the frontside. The mobile phone camera was placed to the left with respect to the THz imager. The green arrows indicate the locations of the nonfunctional channels visible as dark horizontal lines in THz imagery. (e) Plastic rods fabricated from POM material with diameters of 30 and 16 mm were used in imaging situations of (a)–(c) and (d), respectively.

other features such as the nose of the test person in Fig. 7(b) can be observed. Thus, the results demonstrate the performance of the fully staring imaging system for concealed object detection down to the spatial resolution of 16 mm, in line with separate characterization measurements presented in Fig. 6(a), and with a sufficient sensitivity level as predicted by the radiometric contrast measurements shown in Fig. 6(b) [29].

V. CONCLUSION

In conclusion, we have demonstrated, to our knowledge for the first time, a passive THz imaging system with a fully staring detector array for the application of person security screening. Furthermore, this was also the first demonstration of imaging performed with KIBs in the first place. A general tradeoff analysis on the instrument design was given. Besides constraints derived from subsystem-specific properties, there are also general factors contributing to the instrument design, including the instrument weight, size, power consumption, and, of course, the price along with the limitations set by the microfabrication techniques. Another benefit of the fully staring imager is the possibility for a higher video frame rate, in our case restricted by the frame time τ_F , as compared to other systems where scanning mechanics is often a limiting factor.

The question is whether the fully staring concept based on KIBs has potential in emerging commercial applications. Currently, millimeter-wave scanners are in common use in the airport security while potential applications are also found in other mass transit hubs, and loss prevention, to name a few. These may benefit from new approaches, especially those allowing a walk-through type imaging scenarios. Furthermore, the possibilities of the active and passive imaging, or even the combination of the two, are yet to be fully explored [30]. Regarding standoff imaging in general, the imaging geometry is to be optimized for a given application. While the LASTKID system was designed for a short-range imaging distance of 2.5 m, a longer range imaging is equally possible with the KIB technology [15]. Here, the imaging experiments were performed with rather limited imaging area of $0.66 \times 0.86 \text{ m}^2$, while for the LASTKID system, a FOV of $2 \times 1 \text{ m}^2$ is realizable with further scale-up of the electronics. This already enables the imaging of human-sized objects, whereas screening a larger number of people requires larger FOV. Increasing the FPA size eventually leads also to a larger aperture size which, due to the stronger radiative load, sets stringer requirements for the cryogenics. A further optimization of the cryogenic system and advancements in thermal filtering could help to solve these issues.

ACKNOWLEDGMENT

The authors would like to thank Markus Grönholm for the consultation about digital electronics, Paula Holmlund for sample preparation, and Lassi Lehtisyryjä for the help in measurements.

REFERENCES

- [1] D. Barker, D. Hodges, and T. Hartwick, “Far infrared imagery,” *Proc. SPIE*, vol. 67, pp. 27–34, Nov. 1975.

- [2] R. Appleby and H. B. Wallace, "Standoff detection of weapons and contraband in the 100 GHz and 1 THz region," *IEEE Trans. Antennas Propag.*, vol. 55, no. 11, pp. 2944–2955, Nov. 2007.
- [3] K. B. Cooper *et al.*, "THz imaging radar for standoff personnel screening," *IEEE Trans. Terahertz Sci. Technol.*, vol. 1, no. 1, pp. 169–182, Sep. 2011.
- [4] E. Grossman, K. Leong, X. Mei, and W. Deal, "Passive 670 GHz imaging with uncooled low-noise HEMT amplifiers coupled to zero-bias diodes," *Proc. SPIE*, vol. 9078, Jun. 2014, Art. no. 907809.
- [5] E. Heinz *et al.*, "Toward high-sensitivity and high-resolution submillimeter-wave video imaging," *Opt. Eng.*, vol. 50, Nov. 2011, Art. no. 113204.
- [6] S. Rowe *et al.*, "A passive terahertz video camera based on lumped element kinetic inductance detectors," *Rev. Sci. Instrum.*, vol. 87, Mar. 2016, Art. no. 033105.
- [7] A. Luukanen, T. Kiuru, M. Leivo, A. Rautiainen, and J. Varis, "Passive three-colour submillimeter-wave video camera," *Proc. SPIE*, vol. 8715, May 2013, Art. no. 87150F.
- [8] A. Luukanen and J. P. Pekola, "Superconducting antenna-coupled hot-spot microbolometer," *Appl. Phys. Lett.*, vol. 82, pp. 3970–3972, Jun. 2003.
- [9] K. D. Irwin and G. C. Hilton, "Transition-edge sensors," in *Cryogenic Particle Detection*, vol. 99. Berlin: Springer, Jul. 2005, pp. 63–149.
- [10] Asqella Oy, Oct. 2020. [Online]. Available: www.asqella.com
- [11] A. V. Timofeev *et al.*, "Submillimeter-wave kinetic inductance bolometers on free-standing nanomembranes," *Supercond. Sci. Technol.*, vol. 27, Feb. 2014, Art. no. 025002.
- [12] P. K. Day, H. G. LeDuc, B. A. Mazin, A. Vayonakis, and J. Zmuidzinas, "A broadband superconducting detector suitable for use in large arrays," *Nature*, vol. 425, pp. 817–821, Oct. 2003.
- [13] G. Ulbricht *et al.*, "Highly multiplexable thermal kinetic inductance detectors for x-ray imaging spectroscopy," *Appl. Phys. Lett.*, vol. 106, Jun. 2015, Art. no. 251103.
- [14] A. Wandui *et al.*, "Thermal kinetic inductance detectors for millimeter-wave detection," *J. Appl. Phys.*, vol. 128, Jul. 2020, Art. no. 044508.
- [15] A. V. Timofeev *et al.*, "Optical and electrical characterization of a large kinetic inductance bolometer focal plane array," *IEEE Trans. Terahertz Sci. Technol.*, vol. 7, no. 2, pp. 218–224, Mar. 2017.
- [16] H. Sipola *et al.*, "Multiplexed readout of kinetic inductance bolometer arrays," *Rev. Sci. Instrum.*, vol. 90, Feb. 2019, Art. no. 074702.
- [17] C. E. Tucker and P. A. R. Ade, "Thermal filtering for large aperture cryogenic detector arrays," *Proc. SPIE*, vol. 6275, Jun. 2006, Art. no. 62750T.
- [18] D. J. Benford, M. C. Gaidis, and J. W. Kooi, "Optical properties of Zitec in the infrared to submillimeter," *Appl. Opt.*, vol. 42, pp. 5118–5122, 2003.
- [19] J. Hassel *et al.*, "Bolometric kinetic inductance detector technology for sub-millimeter radiometric imaging," *Proc. SPIE*, vol. 9651, Oct. 2015, Art. no. 96510G.
- [20] S. McHugh *et al.*, "A readout for large arrays of microwave kinetic inductance detectors," *Rev. Sci. Instrum.*, vol. 83, Apr. 2012, Art. no. 044702.
- [21] J. C. Mather, "Bolometer noise: Nonequilibrium theory," *Appl. Opt.*, vol. 21, pp. 1125–1129, Mar. 1984.
- [22] E. Gandini, A. Tamminen, A. Luukanen, and N. Llombart, "Wide field of view inversely magnified dual-lens for near-field submillimeter wavelength imagers," *IEEE Trans. Terahertz Sci. Technol.*, vol. 66, no. 2, pp. 541–549, Feb. 2018.
- [23] R. P. Jonas and M. D. Thorpe, "Double Gauss lens design: A review of some classics," *Proc. SPIE*, vol. 6342, Jul. 2006, Art. no. 634202.
- [24] M. J. Griffin, J. J. Bock, and W. K. Gear, "Relative performance of filled and feedhorn-coupled focal-plane architectures," *Appl. Opt.*, vol. 31, pp. 6543–6554, Nov. 2002.
- [25] D. T. Chuss, E. J. Wollack, S. H. Moseley, S. Withington, and G. Saklatvala, "Diffraction considerations for planar detectors in the few-mode limit," *Publ. Astron. Soc. Pac.*, vol. 120, pp. 430–438, Apr. 2008.
- [26] N. Llombart, S. O. Dabironezare, G. Carluccio, A. Freni, and A. Neto, "Reception power pattern of distributed absorbers in focal plane arrays: A fourier optics analysis," *IEEE Trans. Antennas Propag.*, vol. 66, no. 11, pp. 5990–6002, Nov. 2018.
- [27] S. O. Dabironezare *et al.*, "A dual-band focal plane array of kinetic inductance bolometers based on frequency-selective absorbers," *IEEE Trans. Terahertz Sci. Technol.*, vol. 8, no. 6, pp. 746–756, Nov. 2018.
- [28] C. Dietlein, Z. Popovic, and E. N. Grossman, "Aqueous blackbody calibration source for millimeter-wave/terahertz metrology," *Appl. Opt.*, vol. 47, pp. 5118–5122, Oct. 2008.

- [29] C. R. Dietlein, A. Luukanen, F. Meyer, Z. Popovic, and E. N. Grossman, "Phenomenology of passive broadband terahertz images," in *Proc. 4th ESA Workshop Millimetre-wave Technol. Appl.*, 2006, pp. 405–409.
- [30] R. Appleby, H. Petersson, and S. Ferguson, "Concealed object stand-off real-time imaging for security: CONSORTIS," *Proc. SPIE*, vol. 9462, May 2015, Art. no. 946204.



Juho Luomahaara received the M.Sc. (Tech.) degree in engineering physics from the Helsinki University of Technology, Espoo, Finland, in 2009, and the D.Sc. (Tech.) degree in microtechnology and nanotechnology from Aalto University, Helsinki, Finland, in 2014.

He joined VTT, Espoo, Finland, in 2008, where he is now working as a Research Scientist. His research activities have mainly concentrated on superconducting sensors and their applications. During his doctoral research, he studied and developed new superconducting sensors and sensor instrumentation for a combined magnetoencephalography–magnetic resonance imaging system, as well as for a quantum metrology triangle experiment. Currently, he holds a Postdoctoral Fellowship of Academy of Finland with a focus on cryogenic THz detectors and instrumentation.



Hannu Sipola received the M.Sc. (Tech.) degree in electrical engineering from the Helsinki University of Technology (currently Aalto University), Espoo, Finland, in 1990.

In 1991, he joined the Measurement Technology Team, VTT, Espoo, Finland. He has been actively developing low-noise electronics and measurement systems for various technologies, including microelectromechanical systems (MEMS), superconducting quantum interference devices (SQUIDs), THz cameras, and optically pumped magnetometers (OPMs). He is currently a Senior Scientist with the Quantum Systems Team, VTT.



Leif Grönberg (Life Member, IEEE) received the M.Sc. (Tech.) and Lic.Sc. (Tech.) degrees in electrical engineering from the Helsinki University of Technology (currently Aalto University), Espoo, Finland, in 1980 and 1984, respectively.

In 1986, he joined the Superconducting Device Group, VTT, Espoo, Finland. He was actively involved in developing the Nb/Al-AIO/Nb Josephson junction technology for VTT SQUIDs. He has been the Principal Investigator of the fabrication technology for SQUID and terahertz systems; the former has

been commercialized in MEG systems and the latter in THz cameras for security imaging. He has also been working with process development and fabrication of thin-film devices for various applications. He is currently a Senior Scientist with the Quantum Systems Team, VTT.



Aki Mäyrä received the M.Sc. degree in physics from Oulu University, Oulu, Finland, in 2006.

From 2007 to 2008, he was involved with a gravity field and steady-state ocean circulation explorer satellite project with the European Space Research and Technology Centre. Since 2009, he has been a Research Scientist with the VTT Optical Measurements Group, Oulu, Finland, where he has been responsible on optics for several national and EU-funded projects, including design of optics for special applications and system engineering of optical analyzers and measurement devices.

Mika Aikio, photograph and biography not available at the time of publication.



Andrey Timofeev received the M.Sc. degree in physics from Moscow State University, Moscow, Russia, in 2004, and the D.Sc. (Tech.) degree in engineering physics from the Helsinki University of Technology, Espoo, Finland, in 2009.

Since 2009, he has been working as a Research Scientist with VTT, Espoo, Finland. He has specialized in superconducting THz detectors and cameras, tunnel junction quantum devices, and silicon thermoelectric devices. During his Academy of Finland's Postdoctoral Fellowship (2011–2013), he developed

kinetic inductance bolometer technology at VTT. Since 2017, he has been with the Centre for Quantum Computation and Communication Technology, UNSW, Sydney, Australia.



Kirsi Tappura received the M.Sc. (Tech.) (with distinction), Lic.Sc. (Tech.), and D.Sc. (Tech.) degrees in technical physics from the Tampere University of Technology (TUT; currently Tampere University, TAU), Tampere, Finland, in 1990, 1992, and 1993, respectively.

She continued her research on semiconductor physics and optoelectronics at TUT as a Research Scientist and a Project Manager as well as a Postdoctoral Research Fellow of the Academy of Finland, until she joined the Nokia Research Center, Tampere,

Finland, where she was a Senior Research Scientist involved in novel electronic displays. Since late 1997, she has been with the VTT Technical Research Centre of Finland Ltd., Espoo/Tampere, Finland, first, as a Research Scientist, since 1999 as a Senior Scientist, and since 2011 as a Principal Scientist. She was also a Team Leader of modeling, sensors, and energy materials related teams during 1999–2001, 2006–2011, and 2012, respectively. She is currently a Principal Scientist with the Quantum Systems Team, VTT. Since 1999, she has also been a Docent of Physics with TUT/TAU. Her current research interests include the electromagnetic (including plasmonic), electronic, and thermal properties of devices for various applications such as sensing, detection/imaging, energy harvesting, and electro-optic communication with an emphasis on computational physics.

Anssi Rautiainen, photograph and biography not available at the time of publication.



Aleksi Tamminen was born in Ruotsinpyhtää, Finland, in 1982. He received the B.Sc. (Tech.) and M.Sc. (Tech.) degrees from the Helsinki University of Technology, Espoo, Finland, in 2005 and 2007, respectively. He received the Lic.Sc. (Tech.) and D.Sc. (Tech.) degrees in Radio Engineering from Aalto University (former Helsinki University of Technology), Espoo, Finland, in 2011 and 2013, respectively.

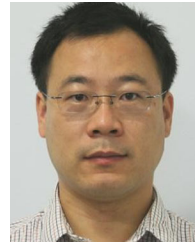
From 2005 to 2013, he was with the Department of Radio Science and Engineering, Aalto University. His research work in Aalto University was related

to antenna measurements and imaging at millimeter and submillimeter waves. In addition to research, he served as the organizing secretary of international conference, *6th ESA Workshop on Millimetre-Wave Technology and Applications* and *4th Global Symposium on Millimeter Waves*, held in Espoo in May 2011. He has authored or coauthored about 40 scientific journals and conference publications as well as three patent applications. From 2013 to 2018, he was Research Scientist with Asqella Ltd., Helsinki, Finland. He was the Principal in the research and development of commercial submillimeter-wave imaging technology as well as in participating in academic research projects in the related field. From 2018, he is with Aalto University as a Research Fellow. His current research interests are submillimeter- and millimeter-wave projects including antenna measurements, sensing biological tissues, and imaging.

Dr. Tamminen was the recipient of the Young Engineer Prize from the *5th European Radar Conference* on November 31, 2008 as well as the Best Student Paper Award from the *Global Symposium on Millimeter Waves 2010* on April 14–16, 2010.

Visa Vesterinen, photograph and biography not available at the time of publication.

Mikko Leivo, photograph and biography not available at the time of publication.



Feng Gao was born in China, in 1977. He received the B.E. degree in photoelectronics and information engineering from the Shandong University, Jinan, China, in 2000, and the M.Sc. degree in microtechnology and nanotechnology from the Helsinki University of Technology, Espoo, Finland, in 2006.

He has been working with VTT Technical Research Centre of Finland, Espoo, Finland, since 2005. His research interests include deep reactive ion etching (DRIE) and general process integration of silicon based MEMS devices.

Hannu Vasama, photograph and biography not available at the time of publication.



Arttu Luukanen was born in Finland, in 1972. He received the M.Sc. degree in applied physics from the University of Helsinki, Espoo, Finland, in 1999, and the Ph.D. degree in applied physics from the University of Jyväskylä, Jyväskylä, Finland, in 2003.

After this, he joined the VTT Technical Research Centre of Finland, Espoo, Finland, as a Research Scientist. From late 2003 until 2005, he worked as a Guest Researcher with the National Institute of Standards and Technology, Boulder, CO, USA. In 2005,

he was appointed as the Director of MilliLab, the millimeter-wave laboratory of Finland, and, in 2009, as the Research Professor of Microsystems and Nanosystems with VTT. From 2007 until 2012, he served on the International Advisory Board of the Swedish FOI-FOCUS Centre of Excellence on Sensors, Multisensors and Sensor Networks, from 2013 until 2016 on the International Advisory Board of the Chalmers GHz Centre, and from 2018 onwards on the Scientific Board of the Aalto University Centre of Quantum Engineering. In 2013, he cofounded Asqella Ltd., Helsinki, Finland, to commercialize passive multiband submillimeter-camera technology, a long time subject of his research. Currently, he serves as the Managing Director of Asqella. His current research interests include mm-wave and THz devices, circuits and imaging systems, as well as turning research into profitable business.

Dr. Luukanen served as the Conference Chair for *SPIE Passive and Active Mmw Imaging Conference* from 2010 until 2016, as the Chair of the Technical Program Committee of the *2012 European Microwave Integrated Circuits Conference*, Conference Chairman of the *6th ESA Workshop on MMW Technology and Applications* in 2011. He is also an elected member of the Finnish Academy of Technical Sciences.



Juha Hassel received the M.Sc. (Tech.) and D.Sc. (Tech.) degrees in engineering physics from the Helsinki University of Technology (currently Aalto University), Espoo, Finland, in 1999 and 2004, respectively.

Since 1999, he has been working with the VTT Technical Research Centre of Finland, Espoo, Finland, as a Research Scientist, as a Senior Scientist since 2008, and as a Principal Scientist since 2015. At VTT, his core research interests included superconducting sensors and electronics for the applications

of medical imaging, THz sensing, and quantum technology. He is also a Docent with Aalto University School of Science, Espoo, Finland, in the field of applied quantum electronics. Currently, he is the Head of System Integration with IQM Quantum Computers, Espoo, Finland.